

## Article

# Dynamic Reliability Analysis of Layered Slope Considering Soil Spatial Variability Subjected to Mainshock–Aftershock Sequence

Huaiming Zhou<sup>1</sup>, Gan Wang<sup>2,3</sup>, Xiang Yu<sup>3</sup> and Rui Pang<sup>2,4,\*</sup> <sup>1</sup> China Communications Investment Nanjing Co., Ltd., Nanjing 210018, China<sup>2</sup> School of Hydraulic Engineering, Faculty of Infrastructure Engineering, Dalian University of Technology, Dalian 116024, China<sup>3</sup> College of Water Conservancy Science and Engineering, Zhengzhou University, Zhengzhou 450001, China<sup>4</sup> State Key Laboratory of Coastal and Offshore Engineering, Dalian University of Technology, Dalian 116024, China

\* Correspondence: pangrui@dlut.edu.cn

**Abstract:** The slope instability brought on by earthquakes frequently results in significant property damage and casualties. At present, the research on displacement response of a slope under earthquake has mainly emphasized the action of the mainshock, without accounting for the impact of an aftershock, and the spatial variability of material parameters is often neglected. The spatial variability of parameters is fully accounted for in this paper, and dynamic reliability of permanent displacement ( $D_P$ ) of a slope produced by the mainshock–aftershock sequence (MAS) is studied. A slope reliability analysis method is proposed based on the Newmark displacement method and the generalized probability density evolution method (GPDEM) to quantify the effect of the spatial variability of materials parameters on dynamic reliability. Firstly, the parameter random field is generated based on the spectral representation method, and the randomly generated parameters are assigned to the finite element model (FEM). In addition, the random simulation method of MAS considering the correlation between aftershock and mainshock is adopted based on the Copula function to generate the MAS. Then, the  $D_P$  of slopes caused by the MAS considering the spatial variability is calculated based on the Newmark method. The impacts of the coefficient of variation (COV) and aftershock on the  $D_P$  of slope is analyzed by means of mean values. Finally, the effect of COV and aftershock on the reliability of  $D_P$  is explained from a probabilistic point of view based on the GPDEM. The results revealed that with the increase in the COV, the mean of the  $D_P$  of the slope shows a trend of increasing gradually. The  $D_P$  of slope is more sensitive to the coefficient of variation of friction angle ( $COV_F$ ). The mean  $D_P$  of the slope induced by the MAS is larger compared to the single mainshock, and the PGA has a significant impact on the  $D_P$ .



**Citation:** Zhou, H.; Wang, G.; Yu, X.; Pang, R. Dynamic Reliability Analysis of Layered Slope Considering Soil Spatial Variability Subjected to Mainshock–Aftershock Sequence. *Water* **2023**, *15*, 1540. <https://doi.org/10.3390/w15081540>

Academic Editor: Georg Ungliger

Received: 16 March 2023

Revised: 8 April 2023

Accepted: 12 April 2023

Published: 14 April 2023

**Keywords:** slope reliability analysis; mainshock–aftershock sequence; spatial variability; Newmark; permanent displacement



**Copyright:** © 2023 by the authors. Licensee MDPI, Basel, Switzerland. This article is an open access article distributed under the terms and conditions of the Creative Commons Attribution (CC BY) license (<https://creativecommons.org/licenses/by/4.0/>).

## 1. Introduction

The instability of slopes brought on by earthquakes is a significant geological risk. Strong earthquakes have a significant impact on large-scale geological disasters, such as landslides and debris flows brought on by slope instability, which frequently result in catastrophic losses and negative social repercussions [1]. It is reported that the Chi-Chi earthquake initiated in excess of 10,000 landslides and slope instability in 11,000 m<sup>2</sup> in Central Taiwan [2]. Around 20,000 people perished in the 2008 Wenchuan earthquake as a result of a large number of landslides and slope instability issues, which made up nearly half of all earthquake fatalities [3,4]. In the Yushu earthquake in 2010, the earthquake created more than 2000 landslides, resulting in a direct economic loss of about CNY 600,000,

8 deaths, and 14 injuries [5]. These aforementioned disaster consequences show that reasonable consideration of dynamic response and sliding displacement of slopes induced by strong earthquakes is very essential for predicting the potential damage possibility of ground motion and conducting rapid seismic risk assessment.

A large amount of historical seismic data has shown the occurrence of strong earthquakes is frequently complemented by multiple aftershocks [6,7]. In the two months after the Wenchuan earthquake in 2008, more than 20,000 aftershocks were triggered, including dozens of strong aftershocks of magnitude 5 or greater. In the three days after the 2013 Lushan earthquake, there were more than 3000 aftershocks and about 4 aftershocks with magnitude stronger than 5 [8]. The spatiotemporal distribution characteristics of aftershocks and mainshocks also play an essential part in influencing the dynamic response of building structures [9]. Hence, it is worthwhile to effectively examine the dynamic response of a slope induced by the MAS. At present, researchers have paid attention to the damage of building structures subjected to the MAS, and more attention has been paid to the dynamic response caused by the combined action of the mainshock and the aftershock with the maximum magnitude. Pang et al. [10] discussed the susceptibility of a CFRD with a height of over 200 m produced by the MAS based on the multiple analysis. Zhou et al. [11] investigated the association between the intensity parameters of ground motion and the structural destruction under the MAS, and established the damage prediction model of the MAS based on the optimal parameters. Based on the Copula theory, Shen et al. [12] established a sequential random model of ground motion that can better represent the spatial correlation of sequential earthquakes. However, there are few studies on the response characteristics of slope caused by mainshock–aftershock sequence at present. In addition, the repeated method is mostly used to construct artificial mainshock–aftershock sequences in the above research, which can neither truly reflect the characteristics of the real mainshock–aftershock sequence nor properly consider the association between the aftershock and mainshock intensity. Therefore, the effect of an aftershock on the structural dynamic response cannot be reasonably responded to. The researchers cannot really grasp the safety of the slope when it is further subjected to an aftershock after the mainshock's initial damage due to the lack of research on the response of the slope induced by the MAS. Therefore, the advanced stochastic simulation method of the MAS requires of further investigation.

In order to consider the seismic slip danger of slopes, many methods have been developed, such as statistical analysis, the permanent displacement method, the pseudo-static method, the safety factor method, and the stress–deformation method [13–16]. Compared with the safety factor method, the permanent displacement caused by seismic action can assess the damage condition and seismic performance of the slope more reasonably [17–19]. In addition, traditional slope stability analysis methods are in general primarily based on deterministic analysis, which considers a series of elements affecting the slope stability as definitive factors. However, a many disaster results and geotechnical tests have revealed the apparent stochastic nature of variables affecting slope stability, such as external load, performance of materials, and model geometry [20–22]. Calculating and analyzing the stability of slopes by using deterministic methods can create many errors. The adoption of reliability theory has provided the opportunity of quantitative consideration of uncertainties in recent years [23,24]. By establishing extreme state equations, metrics such as probability of failure and reliability are employed to describe the safety of systems, thus providing a more complete guide for engineering design. Some traditional probabilistic methods, such as the First Order Second Moment method [25], the Monte Carlo method [26], the response surface method [27], and their improved forms, have been used to analyze the reliability of results and proven to be effective [28]. However, these methods have the characteristics of having difficulty obtaining the random dynamic information of the structure, a huge calculation scale, and a need to be coupled with the structural response analysis and continuous sample training and iteration. Therefore, it is demanding and challenging to apply the seismic random dynamic response and probability analysis of slopes with strong nonlinearity, complex problems, and a large calculation scale. The GPDEM is

a newly developed method for probabilistic analysis [29,30]. At present, the GPDEM has been implemented for dynamic reliability assessment of bridges, slopes, earth-rock dams, and other engineering structures, and its efficiency has been confirmed by comparing it with the MCS method [30–34]. However, the feasibility of GPDEM in the evaluation of slope  $D_P$  caused by a mainshock–aftershock sequence needs further verification.

Soil parameters have significant spatial variability due to differences in depositional conditions, loading history, and other geological processes [35–37]. Moreover, the soil parameters at different spatial locations have a certain relevance and are not completely independent, which makes the slope stability research more complex. In slope reliability analysis, two methods are generally adopted to imitate the variability of soil parameters. Assuming that the parameters are spatially homogeneous, the probability distribution model is applied to describe the inherent variability, which is called random variable model [38,39]. The random variable model assumes that the parameters in the study area are perfectly correlated and that differences in the physical and mechanical properties of the local and overall geotechnical properties at different points in space cannot be considered. This obviously does not conform to the actual situation of geotechnical engineering and cannot meet the needs of objective analysis and evaluation of the spatial variation characteristics of geotechnical parameters. The random field theory was first proposed and adopted by Cornel to describe the random characteristics of parameters in 1972 [40]. On this basis, the theory was gradually developed and refined by Vanmarcke [41]. The main idea is to treat the soil parameters at a certain location in the space as random variables subject to certain statistical laws and describe the spatial variability of soil parameters at different locations through variance reduction function, correlation distance, correlation function, etc. In contrast, the spatial variability of soil material parameters would be better depicted by the random field theory.

In this paper, a slope reliability analysis method based on the GPDEM and the Newmark displacement method is proposed to quantify the effect of spatial variability of soil parameters on dynamic reliability. The MAS and random field are generated by the random simulation method of MAS and the spectral representation method (SRM), and the  $D_P$  of the slope is obtained by a nonintrusive analysis. Firstly, the impact of COV on a slope’s dynamic stability is investigated from the mean value of  $D_P$ , and then the influence of COV and PGA on a slope’s dynamic reliability is explained from a probabilistic point of view by combining the GPDEM. The flowchart of the evaluation framework is depicted in Figure 1.

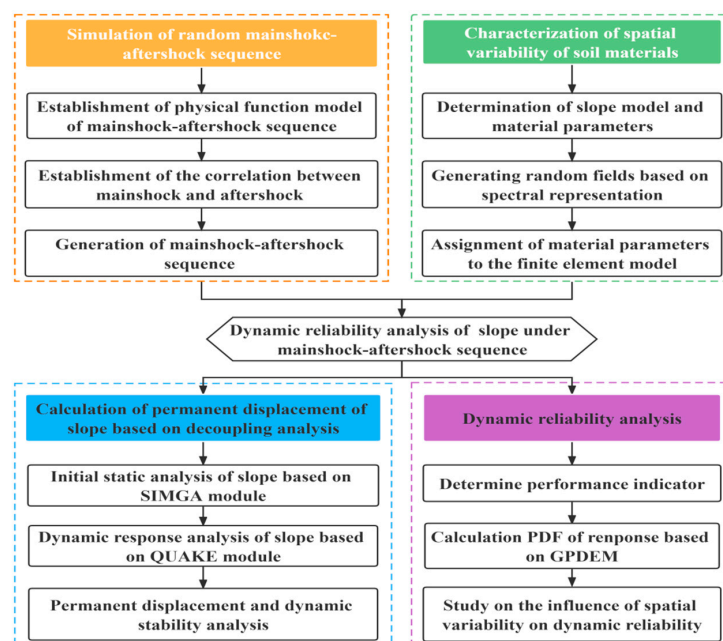


Figure 1. The flowchart of the evaluation framework.

## 2. Generalized Probability Density Evolution Method

This paper considers the spatial variability of layered slope material parameters. Therefore, the slope dynamic equation under the action of MAS may be represented as:

$$\overline{M}(\Theta)\ddot{X}(t) + C(\Theta)\dot{X}(t) + K(\Theta)X(t) = -\overline{M}\ddot{X}_g(\Theta, t) \tag{1}$$

where,  $K$ ,  $C$ , and  $\overline{M}$  represent the stiffness matrices, damping, and effective mass of the structure, respectively, and their basic parameters may be random.

For convenience, the solution of Equation (1) can be formulated as:

$$X(t) = H(\Theta, t) \tag{2}$$

where  $H = (H_1, H_2, \dots, H_n)^T$ ;  $n$  is the number of degrees of freedom. In addition, it is worth noting that it can be regarded as a variable  $\Theta$  and  $t$ .

Accordingly, variables such as acceleration, velocity, strain, and stress could also be expressed in the form similar to Equation (2). Therefore, in order to be more general, we can uniformly express the physical quantities of interest in the following form:

$$Z(t) = H_z(\Theta, t) \tag{3}$$

where  $H_z = (H_{z,1}, H_{z,2}, \dots, H_{z,m})^T$ .

Under the framework of probability conservation, the generalized probability density evolution equation of the stochastic process may be represented as:

$$\frac{\partial p_{z\Theta}(z, \theta, t)}{\partial t} + \sum_{l=1}^m \dot{Z}_l(\theta, t) \frac{\partial p_{z\Theta}(z, \theta, t)}{\partial z_l} = 0 \tag{4}$$

where  $p_{z\Theta}(z, \theta, t)$  is the joint probability density function of the system  $(z, \Theta)$ , and  $m$  is the dimension of the equation, independent of the number of degrees of freedom of the system  $n$ .

$$\frac{\partial p_{z\Theta}(z, \theta, t)}{\partial t} + \dot{Z}(\theta, t) \frac{\partial p_{z\Theta}(z, \theta, t)}{\partial z_l} = 0 \tag{5}$$

$$p_{z\Theta}(z, \theta, t)|_{t=t_0} = \delta(z - z_0)p_{\Theta} \tag{6}$$

$$p_{z\Theta}(z, \theta, t)|_{z_j \rightarrow \pm\infty} = 0, j = 1, 2, 3, \dots, m \tag{7}$$

If only a single physical quantity is considered, Equation (4) is simplified to the form of Equation (5). Combining the initial conditions represented by Equation (6) and the boundary conditions represented by Equation (7), the structural reliability is finally obtained through mathematical processing. For simple problems, the analytical solution can be obtained in this way. For complex problems, such as large complex nonlinear systems, the numerical solution can only be obtained by mathematical methods, which could be achieved by the procedure as follows:

- (1) Point selection and probability assignment in probability space.

Discrete representative points are selected by some means in  $\Omega_{\Theta}$  of random variables (such as the number-theory method, the point-selecting method by cutting the ball, the quasi-rotational symmetry point method, and the GF-deviation method).

- (2) Deterministic solutions for dynamic systems.

The physical Equations (1) and (3) are solved, and the velocity of the required physical quantity is found for each given  $\Theta = \theta_q$ .

- (3) Solving probability density evolution equation.

After the representative points are selected and the probabilities are assigned in step (1), the Equation (4) is transformed into:

$$\frac{\partial p_{z\Theta}(z, \theta_q, t)}{\partial t} + \sum_{j=1}^m \dot{Z}_j(\theta_q, t) \frac{\partial p_{z\Theta}(z, \theta_q, t)}{\partial z_j} = 0 \tag{8}$$

The corresponding initial conditions are transformed into:

$$p_{z\Theta}(z, \theta_q, t) \Big|_{t=t_0} = \delta(z - z_0) P_q \tag{9}$$

The result of the partial differential equation can be obtained by substituting  $\dot{Z}(\theta_q, t_m)$ , as obtained in step (2), into Equations (8) and (9).

(4) Cumulative summation.

The result of  $p_z(z, t)$  is acquired by the summation of all the above single results  $p_{z\Theta}(z, \theta_q, t)$ .

$$p_z(z, t) = \sum_{q=1}^{n_{sel}} p_{z\Theta}(z, \theta_q, t) \tag{10}$$

### 3. Simulation of Random Field and Random Main Aftershock Sequence

#### 3.1. Spectral Representation Method

Many methods are currently employed to decompose random fields, for example, the midpoint method [42], spectral representation method [43], the spatial averaging method [44], the K-L decomposition method [45], and other methods. The spectral representation method has gradually become a widely used random field simulation method because of its good speed and accuracy in convergence to the objective function, and the generated sample function has ergodicity in all states.

By using the spectral representation method [43], the establishment of one-dimensional stationary random field could be expressed as:

$$\hat{f}(x_1) = \sqrt{2} \sum_{n=0}^{N-1} A_n \cos(\kappa_n x + \Phi_n) \tag{11}$$

where  $\Phi_n$  is the independent phase angle uniformly distributed within the region of  $[0, 2\pi]$ ;  $A_n$  is the amplitude; and  $\kappa_n$  is the frequency.

$$A_n = \sqrt{2S_{ff}(\kappa_n)\Delta\kappa} \tag{12}$$

$$\kappa_n = n\Delta\kappa = n \frac{\kappa_u}{N} \tag{13}$$

where  $\kappa_u$  denotes the number of truncated waves;  $n = 0, 1, 2, \dots, N - 1$ .

In Equation (12),  $S_{ff}(\kappa_n)$  is the power spectrum function. The relationship between  $S_{ff}(\kappa_n)$  and autocorrelation function can be acquired by Fourier transform, as shown below:

$$S_{ff}(\kappa) = \frac{1}{2\pi} \int_{-\infty}^{\infty} \rho_{ff}(\xi) e^{-i\kappa\xi} d\xi \tag{14}$$

Note that:

$$A_0 = 0 \text{ or } S_{ff}(\kappa_0) = 0 \tag{15}$$

The two-dimensional stationary random field can be characterized as:

$$f(x_1, x_2) = \sqrt{2} \sum_{n_1=0}^{N_1-1} \sum_{n_2=0}^{N_2-1} \left[ A_{n_1 n_2} \cos(\kappa_{1n_1} x_1 + \kappa_{2n_2} x_2 + \Phi_{n_1 n_2}^{(1)}) + \tilde{A}_{n_1 n_2} \cos(\kappa_{1n_1} x_1 - \kappa_{2n_2} x_2 + \Phi_{n_1 n_2}^{(2)}) \right] \tag{16}$$

where  $\Phi_{n_1 n_2}^{(1)}$  and  $\Phi_{n_1 n_2}^{(2)}$  are individual random phase angles uniformly distributed within region of  $[0, 2\pi]$ ;  $A_{n_1 n_2}$  and  $\tilde{A}_{n_1 n_2}$  are amplitude;  $\kappa_{1n_1}$  and  $\kappa_{1n_2}$  are frequency.

$$A_{n_1 n_2} = \sqrt{2S_{f_0 f_0}(\kappa_{1n_1}, \kappa_{2n_2}) \Delta\kappa_1 \Delta\kappa_2} \tag{17}$$

$$A_{n_1 n_2} = \sqrt{2S_{f_0 f_0}(\kappa_{1n_1}, -\kappa_{1n_2}) \Delta\kappa_1 \Delta\kappa_2} \tag{18}$$

$$K_{1n_1} = n_1 \Delta\kappa_1 = \frac{\kappa_{1u}}{N_1} \tag{19}$$

$$K_{2n_2} = n_2 \Delta\kappa_2 = \frac{\kappa_{2u}}{N_2} \tag{20}$$

where  $\kappa_{1u}$  and  $\kappa_{2u}$  denote the number of truncated waves and meet the following relationship:

$$\begin{cases} -\kappa_{1u} \leq \kappa_1 \leq \kappa_{1u} \\ -\kappa_{2u} \leq \kappa_2 \leq \kappa_{2u} \end{cases} \tag{21}$$

In Equation (17),  $S_{f_0 f_0}(\kappa_1, \kappa_2)$  is the power spectrum function. The relationship between  $S_{f_0 f_0}(\kappa_1, \kappa_2)$  and autocorrelation function can be obtained through Fourier transform, as shown below:

$$S_{f_0 f_0}(\kappa_1, \kappa_2) = \frac{1}{(2\pi)^2} \int_{-\infty}^{\infty} R_{f_0 f_0}(\xi_1, \xi_2) e^{-i(\kappa_1 \xi_1 + \kappa_2 \xi_2)} d\xi_1 d\xi_2 \tag{22}$$

### 3.2. Generation of Parametric Random Fields Based on Spectral Representation Method

In the random field simulation of slope strength parameters, since the value of strength parameters is usually positive, lognormal random field is employed to simulate the spatial difference and correlation of material parameters. The logarithmic stationary random field of slope strength parameters is established based on Equation (16).

$$\omega(x, z) = \exp\left(\xi_{\ln} \cdot \sum_{i=0}^{M-1} \sum_{j=0}^{N-1} \sigma_{ij} [V_{ij}(\theta) \cos(\omega_{1i}x + \omega_{2j}z) + W_{ij}(\theta) \sin(\omega_{1i}x + \omega_{2j}z) + \lambda_{\ln}]\right) \tag{23}$$

where the  $V_{ij}(\theta)$  and  $W_{ij}(\theta)$  are mutually independent and obey the standard normal distribution;  $\omega_{1i}$  and  $\omega_{2j}$  are frequency coordinate values.  $x$  and  $z$  are the horizontal and vertical coordinate values of space.  $\xi_{\ln}$  and  $\lambda_{\ln}$  are the logarithmic standard deviation and logarithmic mean of parameters.  $\sigma_{ij}$  is the standard deviation of  $i * M + j + 1$ .

$$\begin{cases} \lambda_{\ln} = \ln(\mu) - 0.5 \cdot \ln(1 + \text{cov}^2) \\ \xi_{\ln} = \sqrt{\ln(1 + \text{cov}^2)} \end{cases} \tag{24}$$

$$\sigma_{ij} = \sqrt{4S_{\omega\omega}(\omega_{1i}, \omega_{2j}) \cdot \Delta\omega_1 \cdot \Delta\omega_2} \tag{25}$$

where  $S_{\omega\omega}$  is the power spectral density function corresponding to the correlation function, which can be obtained by two-dimensional Fourier transform of the autocorrelation function.

$$S_{\omega\omega}(\omega_1, \omega_2) = \frac{1}{(2\pi)^2} \int_{-\infty}^{+\infty} \int_{-\infty}^{+\infty} \rho(x, z) e^{-i(\omega_1 x + \omega_2 z)} dx dz \tag{26}$$

where  $\rho(x, z)$  is the autocorrelation function. The Gaussian autocorrelation function with good stability and continuity is used for calculation.  $\Delta\omega_1$  and  $\Delta\omega_2$  are the discrete intervals of the frequency coordinate axes  $\omega_1$  and  $\omega_2$ , respectively.

### 3.3. Random Simulation of Mainshock–Aftershock Sequence (MAS)

Due to the limited number of measured records, it is necessary to generate the MAS ground motion through artificial simulation for seismic analysis of engineering structures. The existing method for constructing the MAS is to develop the magnitude relationship between the mainshock and aftershock and then separate and adjust the actual ground motion records (or artificial ground motion) to obtain the time histories of the MAS. However, in addition to the magnitude, the mainshock and aftershock are intimately associated in respect to source, propagation path, and local site impact, i.e., they are highly correlated in terms of spectrum characteristics, ground motion intensity, and duration. Obviously, a single magnitude parameter cannot accurately reflect the characteristics of the MAS. In addition, by adjusting the recorded ground motion or adopting the ground motion model of single shock, the changes of the amplitude, duration, and frequency spectrum of ground motion in the process of seismic wave propagation cannot be well reflected. Therefore, a random MAS simulation method accounting for the relevance between aftershock and mainshock based on Copula function is adopted to generate the MAS. This approach is characterized in greater depth in previous studies [46], and the primary steps of the approach can be simplified as follows:

- (1) Establishment of a physical random function model of the MAS.
- (2) The real MASs are collected from the PEER to determine the physical parameters in the physical random function model of the mainshock–aftershock sequence.
- (3) Select a representative set of points of seismic parameters according to the GF difference. Then, establish the relevance between the aftershock and mainshock parameters based on the Copula theory.
- (4) Generate a series of random MASs by using the narrowband harmonic superposition method.

## 4. Nonintrusive Analysis of Slope Dynamic Reliability

The biggest advantage of noninvasive randomness analysis is that the process of deterministic analysis and randomness analysis are independent of each other. The FE method is adopted to perform deterministic analysis without modifying the finite element kernel; therefore, the integration of deterministic analysis and stochastic analysis is realized, which significantly improves the reliability of the stochastic analysis results. By combining dynamic reliability analysis with finite element batch processing, this paper proposes a nonintrusive analysis frame of slope reliability considering spatial variability subjected to the MAS and compiles the interface program between dynamic reliability analysis and GeoStudio finite element software.

- (1) Establish the slope of the FE model, divide the model mesh, set the boundary conditions, define the load loading method, define the material properties, and assign the elements in the SIGMA/W module with the parameter averages. Then, establish the corresponding relationship between the elements, groups, and material properties. Additionally, establish the stability analysis model in SLOPE/W, and save the FEM as a file with the extension name of “.xml”.
- (2) The slope strength parameters are simulated by the spectral representation method. N groups of data of parameters will be generated, and the parameters in the “.xml” file will be replaced in batches with the newly generated n groups of data through MATLAB programming to obtain n new “.xml” files.
- (3) Use the UE text editor software to directly use GeoStudio to batch calculate the stability of the n new “.xml” files obtained in step (2). Then, output the calculation result files corresponding to each group of parameters.
- (4) The calculation results corresponding to all parameter groups are extracted in batch, and the  $D_P$  is statistically analyzed.

## 5. Model Establishment and Material Parameters

### 5.1. Finite Element Model

In this study, the FEM adopted is a simplified layered soil slope based on geological data and field survey along the G317 Sichuan–Tibet Highway. The two-dimensional FEM was adopted to carry out the dynamic reliability analysis of layered soil slope. As demonstrated in Figure 2, the layered soil slope model is 40 m long and 24 m high. The FEM has been used in other studies to research the failure mode of a slope through numerical simulation and model tests [47]. In this study, two different types of layered soil slopes are used to research the dynamic reliability of the slope considering the spatial variability subjected to the MAS. The size of the grid is chosen to be 0.5 m, which ensures both computational efficiency and accuracy. Other information about the finite element model is introduced in detail in previous studies [6]. According to different soil layer distribution types, the two layered soil slopes are clayey soil–gravel soil–sandy soil–foundation soil and clayey soil–sandy soil–gravel soil–foundation soil. (The soil mass is arranged from top to bottom.)

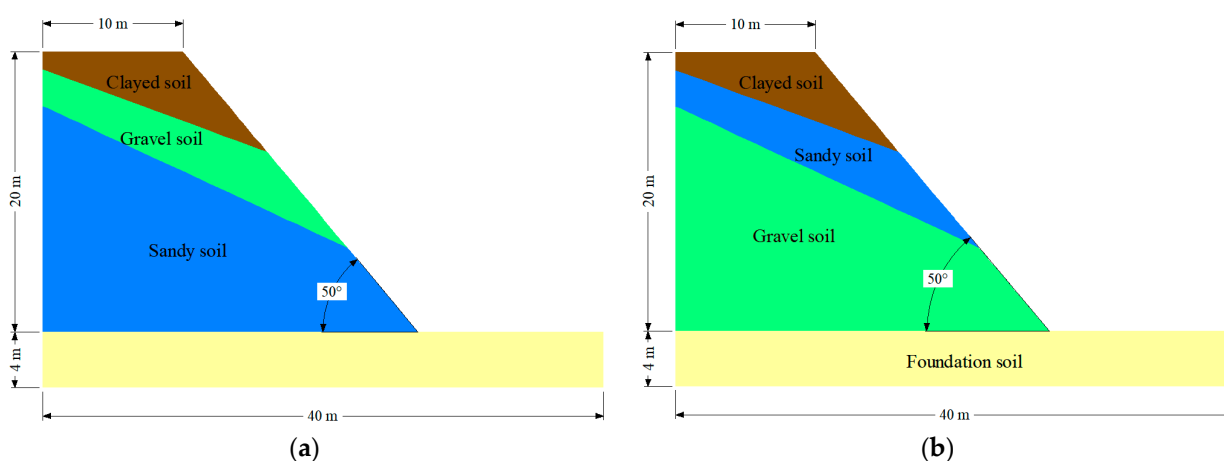


**Figure 2.** Size of finite element model: (a) Case 1; (b) Case 2.

During the initial static analysis and dynamic response analysis of the layered soil slope, the bottom of the FEM is constrained both horizontally and vertically. In addition, the right and left boundaries of the FEM are restrained horizontally during initial static analysis of the slope but not during the dynamic analysis.

### 5.2. Calculation Parameters

Various constitutive models are adopted to characterize the mechanical properties of different soil materials of the layered soil slope. The three layers of soil above the foundation soil are described by the equivalent linear model. The equivalent linear model is applied to the foundation soil because it is compacted. The correlation between damping ratio, shear modulus, and shear strain is presented in Figure 3. The material calculation parameters are the same as those employed by Huang [37], as shown in Table 1.

**Table 1.** Basic parameters of slope soil materials.

Materials	$c$ (kPa)	$\varphi$ ( $^{\circ}$ )	$E$ (MPa)	$\gamma$ (kN/m <sup>3</sup> )	$\nu$
Clayey soil	70.24	24.00	86	22.16	0.35
Sandy soil	13.65	32.50	60	17.23	0.32
Gravelly soil	18.23	38.50	73	19.55	0.3
Foundation soil	200	35.02	800	25.14	0.25

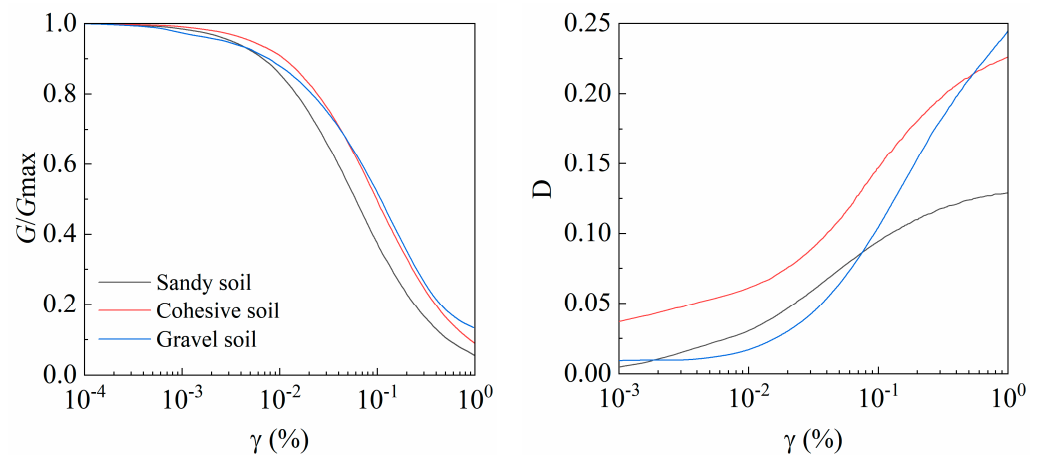


Figure 3. Correlation between damping ratio, shear modulus, and shear strain of materials.

The spatial variability of material is accounted for, and the parameter random field is generated by the above SRM. Then, the parameters are assigned to the well-constructed FEM. In this study, the parameters of each soil layer are presumed as independent of each other. The  $COV$  of  $c$  and  $\varphi$  ( $COV_C$  and  $COV_F$ ) are set as 0.1, 0.2, and 0.3. The vertical and horizontal autocorrelation distances ( $l_h$  and  $l_v$ ) are 20 m and 2 m, respectively. The horizontal dimension of the random field unit is 2 m, and the vertical dimension is 0.5 m. The ratios of the vertical and horizontal fluctuation ranges to the vertical and horizontal dimensions of the random field are  $\delta_h/l_x = 20\sqrt{\pi}/2 = 17.7$  and  $\delta_v/l_y = 2\sqrt{\pi}/0.5 = 7.08$ , respectively, which are greater than the accuracy requirements (5.7~7.6) given by Ching and Phoon [48].

### 5.3. Input of the Mainshock–Aftershock Sequence

One of the randomly generated MAS is employed as the deterministic seismic wave input. The acceleration curve of MAS is presented in Figure 4.

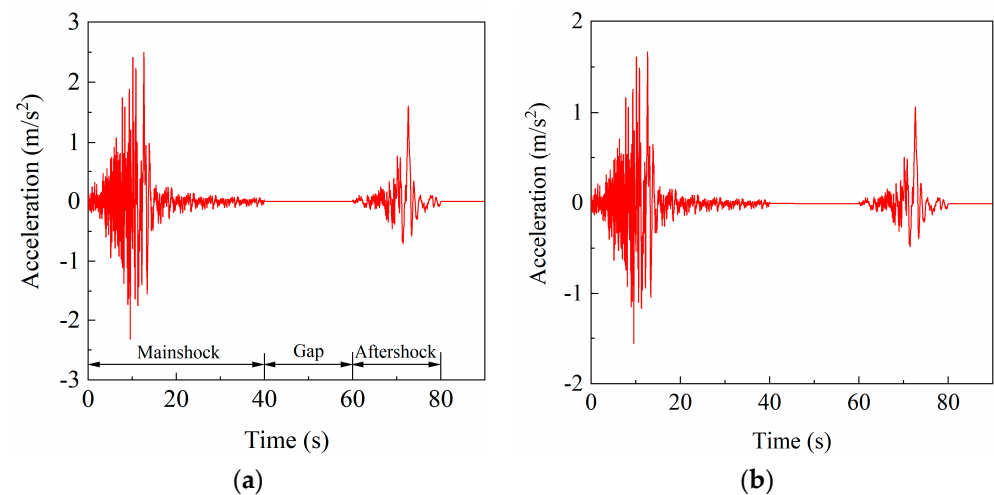


Figure 4. Acceleration change curve of the mainshock–aftershock sequence: (a) horizontal; (b) vertical.

## 6. Effect of Coefficient of Variation on Dynamic Reliability of Layered Soil Slope

The  $D_P$  is adopted to assess the dynamic stability of slope, so it is necessary to define the critical  $D_P$  of the soil slope. According to previous research [6], three  $D_P$  thresholds (0.05 m, 0.5 m, and 1 m) were used to assess the dynamic reliability of the layered slope. A total of 86 sets of random material parameters were generated based on spectral representation to explore the impact of spatial variability on slope dynamic reliability.

6.1. Case 1: Clayey Soil–Gravel Soil–Sandy Soil–Foundation Soil

Figure 5 presents the distribution of  $D_P$  discrete points for Case 1 when the  $COV_C$  values are 0.1, 0.2, and 0.3. It is significant that when the  $COV_C$  is small, the  $D_P$  is small and relatively concentrated. With the increase in  $COV_C$ , the range of variation of soil cohesion increases, the distribution of discrete points of  $D_P$  becomes more discrete, and the mean of  $D_P$  gradually increases. When the  $COV_C$  is 0.1, the mean of  $D_P$  caused by the MAS is 0.63 m, while the mean  $D_P$  for the slope subjected to the single mainshock is 0.339 m. It is obvious that the mean  $D_P$  of the slope induced by MAS is wider than the  $D_P$  caused by the single mainshock. Moreover, the mean  $D_P$  values of the slope under the MAS are 0.668 m and 0.725 m, respectively, when the  $COV_C$  is 0.2 and 0.3. At this time, the mean  $D_P$  of the slope due to the single mainshock is 0.368 m and 0.42 m. The mean value of  $D_P$  increases continuously along with the increment of  $COV_C$ , and the discrepancy of  $D_P$  also shows a gradual tendency to increase.

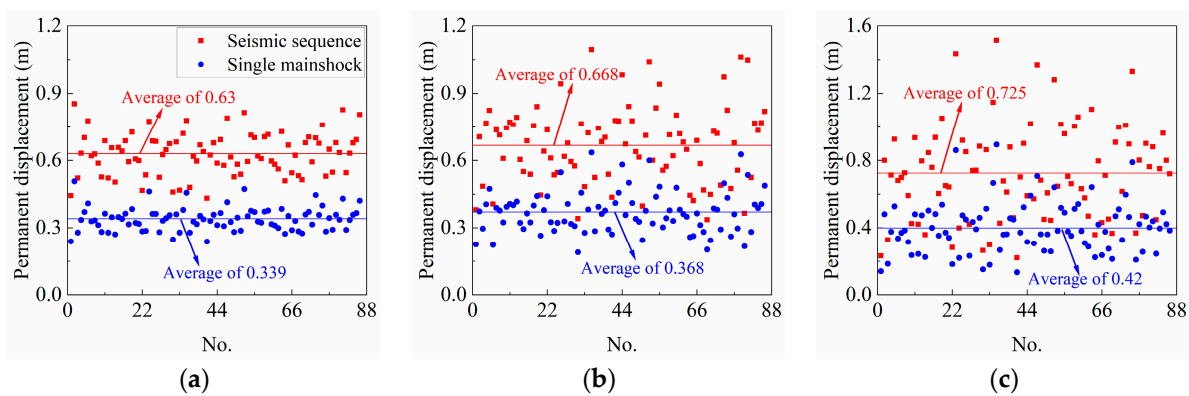


Figure 5. Distribution of discrete points of  $D_P$  under different  $COV_C$  (Case 1): (a)  $COV_C = 0.1$ ; (b)  $COV_C = 0.2$ ; (c)  $COV_C = 0.3$ .

Figure 6 displays the distribution of  $D_P$  discrete points of slope under various PGA when the  $COV_C$  is 0.3. When the PGA values are 0.4 g and 0.6 g, the mean  $D_P$  values of the slope caused by the MAS are 0.386 m and 0.924 m, respectively. However, the mean  $D_P$  values of the slope induced by the single mainshock are 0.224 m and 0.505 m. The  $D_P$  of the slope constantly changed incrementally with the increase in PGA.

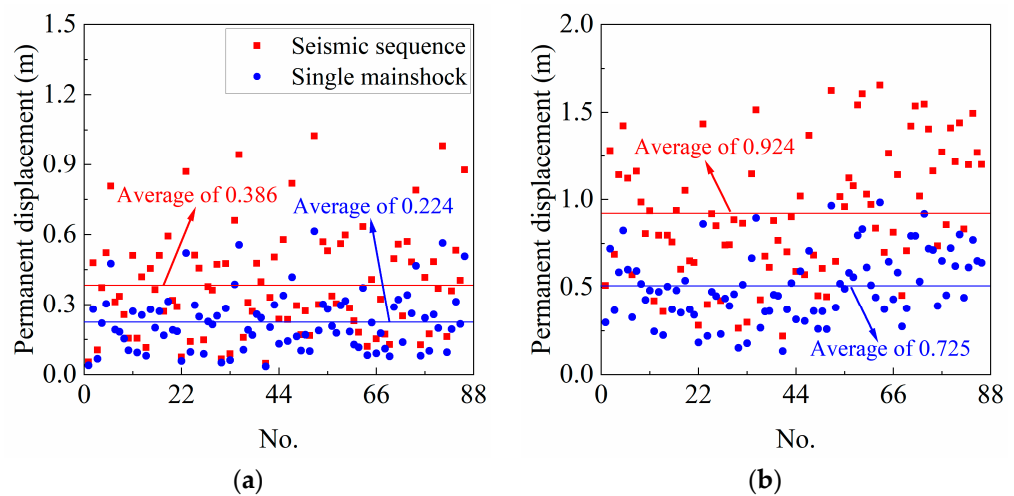


Figure 6. Distribution of discrete points of  $D_P$  under different PGA when  $COV_C=0.3$  (Case 1): (a) PGA = 0.4 g; (b) PGA = 0.6 g.

Figures 7 and 8 show the probability information of  $D_P$  of slope under different  $COV_C$ . When the  $COV_C$  is 0.1, the maximum value of PDF is 3.98, the fluctuation region of  $D_P$

is 0.4–1.0 m, and the  $D_P$  is primarily focused around 0.45 m. When the  $COV_C$  is 0.3, the maximum value of PDF is 1.2, the fluctuation region of  $D_P$  of slope is 0–1.5 m, and the  $D_P$  is relatively centralized around 0.8 m. With the growth of the  $COV_C$ , the PDF value gradually decreases, the curve gradually shifts to the right, the  $D_P$  distribution range is wider, and the failure probability of the slope is higher. Table 2 shows the reliability information of the slope when the cumulative slips are 0.05 m, 0.5 m, and 1 m under different  $COV_C$  and PGA. The dynamic reliability of the slope caused by the MAS decreases by 13% with the  $COV_C$  increasing from 0.1 to 0.3 when the PGA is 0.5 g, and the displacement threshold is 1 m. When the  $COV_C$  is 0.3, the dynamic reliability of the slope under the action of the MAS is also reduced by 13% compared with the single mainshock. In addition, with the PGA increasing from 0.4 g to 0.6 g, the dynamic reliability of the slope induced by MAS decreased by 35%.

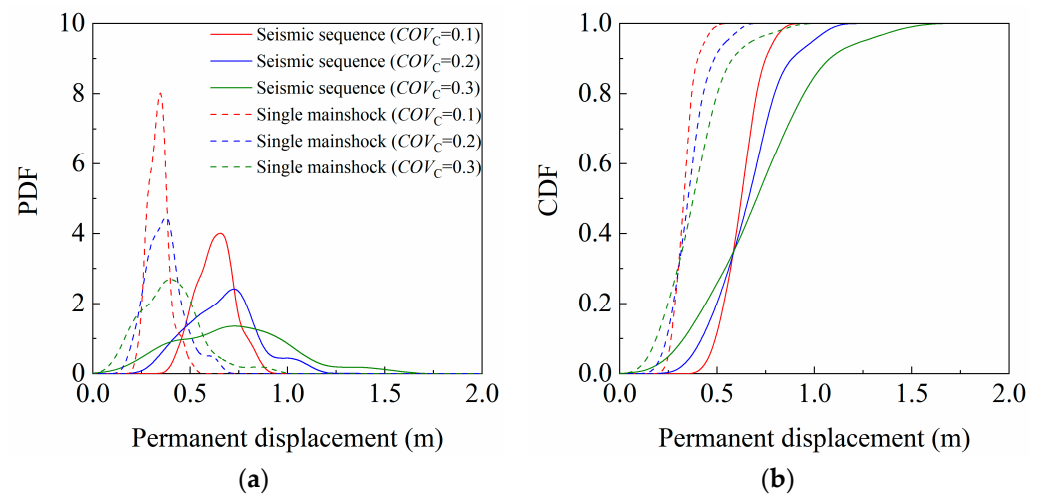


Figure 7. Probability distribution of  $D_P$  with different  $COV_C$  (Case 1): (a) PDF; (b) CDF.

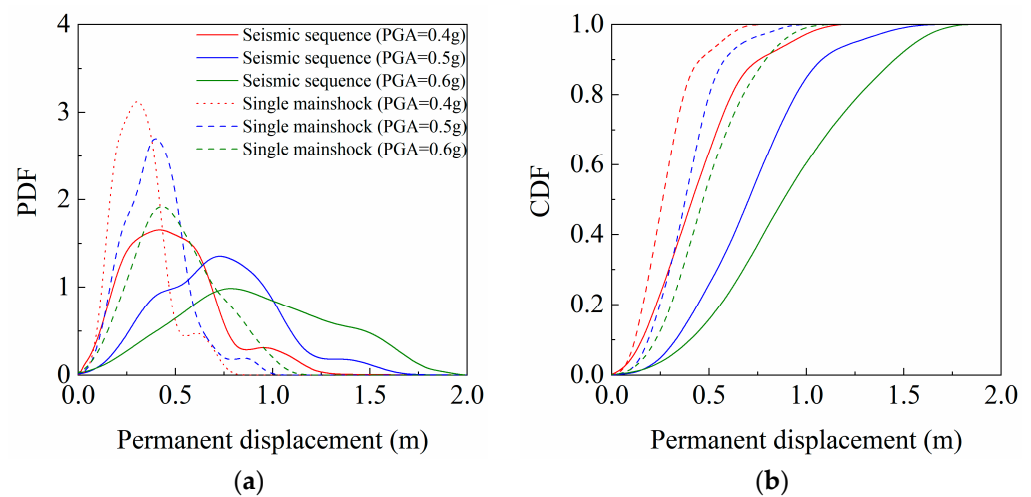


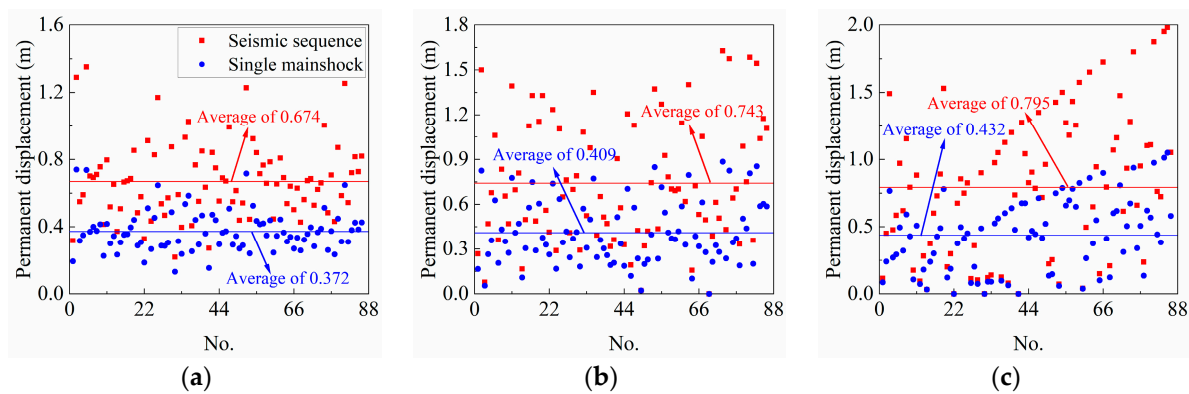
Figure 8. Probability distribution of  $D_P$  with different PGA when  $COV_C = 0.3$  (Case 1): (a) PDF; (b) CDF.

Figure 9 provides the distribution of  $D_P$  discrete points for Case 1 when the  $COV_F$  values are 0.1, 0.2, and 0.3. As the  $COV_F$  is small, the  $D_P$  for the slope is low and concentrated. With the increase in  $COV_F$ , the fluctuating region increases and the mean value of  $D_P$  of slope gradually increases and becomes more discrete. When the  $COV_F$  is 0.1, the mean  $D_P$  of the slope under the MAS is 0.674 m and the mean  $D_P$  of the slope under the single mainshock is 0.372 m. The mean  $D_P$  of the slope induced by the MAS is larger than that

under the single mainshock. When the  $COV_F$  values are 0.2 and 0.3, the mean  $D_P$  values of the slope caused by the MAS are 0.743 m and 0.795 m, respectively. At this time, the mean  $D_P$  values of the slope due to the single mainshock are 0.409 m and 0.432 m. With increasing  $COV_F$ , the mean value of  $D_P$  of the slope continuously increases.

**Table 2.** Dynamic reliability of slope under different  $COV_C$  and PGA (Case 1).

Type of Ground Motion	$D_P$	$COV_C$			PGA		
		0.1	0.2	0.3	0.4 g	0.5 g	0.6 g
Mainshock–aftershock sequence	0.05 m	0	0	0.016	0.035	0.016	0.003
	0.5 m	0.09	0.21	0.26	0.77	0.26	0.15
	1 m	1	0.96	0.87	0.98	0.87	0.63
Single mainshock	0.05 m	0	0	0.016	0.035	0.016	0.003
	0.5 m	0.99	0.92	0.84	0.95	0.84	0.58
	1 m	1	1	1	1	1	1



**Figure 9.** Distribution of discrete points of  $D_P$  under different  $COV_F$  (Case 1): (a)  $COV_F = 0.1$ ; (b)  $COV_F = 0.2$ ; (c)  $COV_F = 0.3$ .

Figure 10 illustrates the distribution of  $D_P$  discrete points of slope under different PGA when the  $COV_F$  is 0.3. When the PGA values are 0.4 g and 0.6 g, the mean  $D_P$  values of the slope subjected to the MAS are 0.41 m and 1.165 m, respectively. However, the mean  $D_P$  value of for Case 2 caused by the single mainshock are 0.246 m and 0.648 m. Obviously, the  $D_P$  of for the slope increases continuously with the growth of PGA.

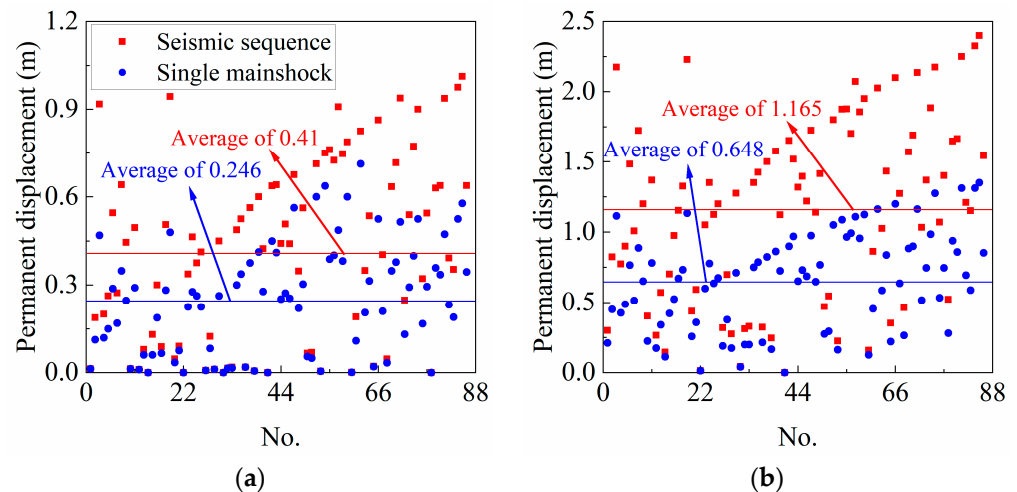


**Figure 10.** Distribution of discrete points of  $D_P$  under different PGA when  $COV_F = 0.3$  (Case 1): (a) PGA = 0.4 g; (b) PGA = 0.6 g.

Figures 11 and 12 show the probability information of the  $D_P$  of the slope under different  $COV_F$  values. The maximum PDF value is 1.89 when the  $COV_F$  is 0.1, and the  $D_P$  of the slope is principally around 0.7 m. With the growth of the  $COV_F$ , the PDF value gradually decreases, and the  $D_P$  of the slope is more widely distributed. Table 3 shows the information of dynamic reliability for the slope when the cumulative slip is 0.05 m, 0.5 m, and 1 m under different  $COV_F$  and PGA. When the PGA is 0.5 g and the threshold is 1 m, the dynamic reliability of the slope induced by the MAS decreases by 25% with the  $COV_F$  increasing from 0.1 to 0.3. When the  $COV_F$  is 0.3, the dynamic reliability of the slope under the action of the MAS is also reduced by 31% compared with the single mainshock. In addition, with the PGA increasing from 0.4 g to 0.6 g, the dynamic reliability of the slope under the MAS decreased by 17%.

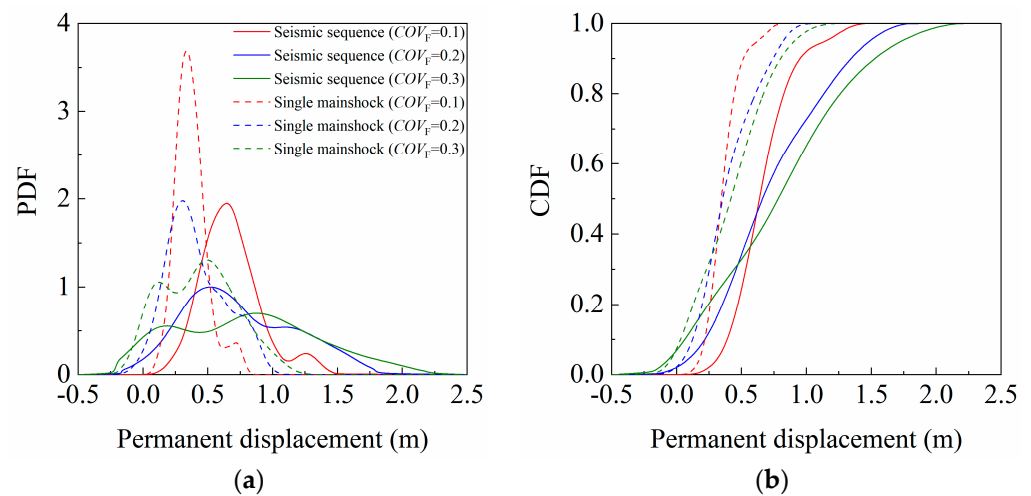


Figure 11. Probability distribution of  $D_P$  with different  $COV_F$  (Case 1): (a) PDF; (b) CDF.

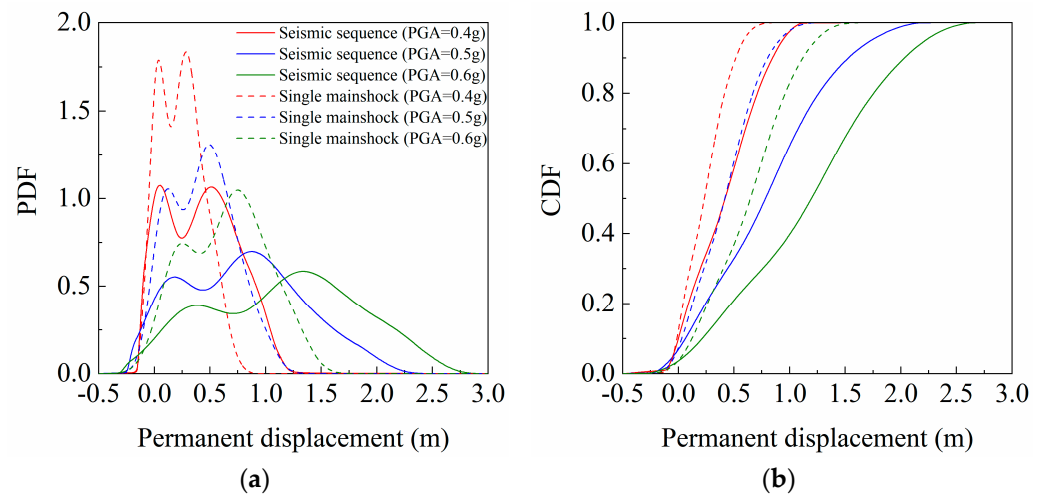


Figure 12. Probability distribution of  $D_P$  with different PGA when  $COV_F = 0.3$  (Case 1): (a) PDF; (b) CDF.

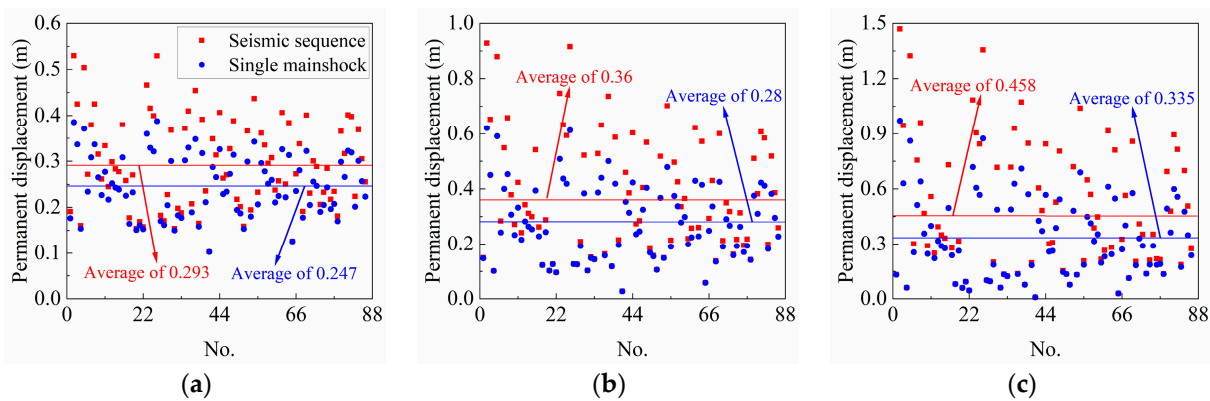
For Case 1, with the increase in  $COV_C$  and  $COV_F$ , the dynamic reliability gradually decreases, and the failure probability gradually increases under different displacement thresholds. In contrast, the dynamic reliability of slopes is more sensitive to  $COV_F$ . Additionally, the dynamic reliability of slopes is more sensitive to the  $COV_F$ . Similar conclusions were also obtained by Huang et al. [1], but the impact of aftershocks was not considered in their research.

**Table 3.** Dynamic reliability of slope under different  $COV_F$  and PGA (Case 1).

Type of Ground Motion	$D_P$	$COV_F$			PGA		
		0.1	0.2	0.3	0.4 g	0.5 g	0.6 g
Mainshock–aftershock sequence	0.05 m	0.01	0.03	0.16	0.23	0.16	0.04
	0.5 m	0.23	0.38	0.32	0.61	0.32	0.24
	1 m	0.92	0.71	0.67	0.99	0.67	0.38
Single mainshock	0.05 m	0.01	0.03	0.16	0.26	0.1	0.04
	0.5 m	0.89	0.88	0.61	0.89	0.61	0.38
	1 m	1	1	0.98	1	0.98	0.83

6.2. Case 2: Clayey Soil–Sandy Soil–Gravel Soil–Foundation Soil

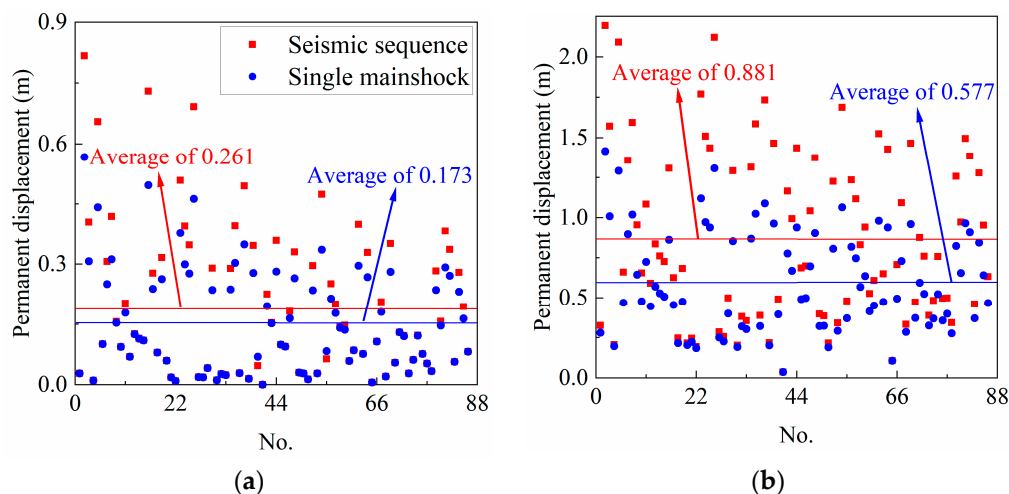
Figure 13 illustrates the dispersion of  $D_P$  dispersion points for Case 2 when the  $COV_C$  values are 0.1, 0.2, and 0.3, respectively. The  $D_P$  of the slope is smaller and more concentrated when the  $COV_C$  is small. With the increase in the  $COV_C$ , the  $D_P$  of the slope is gradually increased and became more discrete. When the  $COV_C$  is 0.1, the mean of  $D_P$  caused by the MAS is 0.293 m, and the mean of  $D_P$  of the slope induced by the single mainshock is 0.247 m. When the  $COV_C$  values are 0.2 and 0.3, the mean of  $D_P$  subjected to the MAS is 0.36 m and 0.458 m, respectively. At this time, the mean of  $D_P$  values under a single mainshock are 0.28 m and 0.335 m. The mean of  $D_P$  increases continuously, and the difference shows a trend of increasing gradually with the increase in the  $COV_C$ .



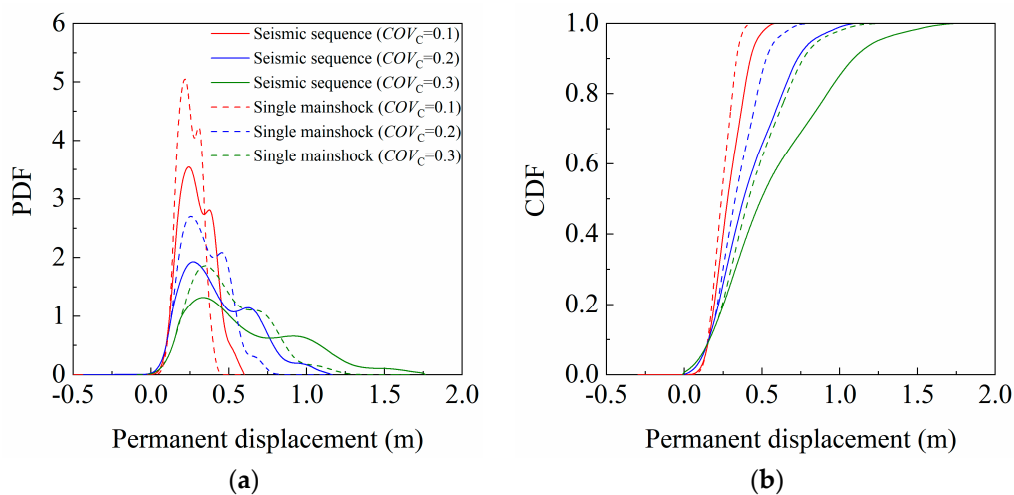
**Figure 13.** Distribution of discrete points of  $D_P$  under different  $COV_C$  (Case 2): (a)  $COV_C = 0.1$ ; (b)  $COV_C = 0.2$ ; (c)  $COV_C = 0.3$ .

Figure 14 summarizes the distribution of  $D_P$  discrete points of the slope under different PGA when the  $COV_C$  is 0.3. When the PGA is 0.4 g and 0.6 g, the mean of  $D_P$  values under the MAS are 0.261 m and 0.881 m, respectively. However, the mean of  $D_P$  values under a single mainshock are 0.173 m and 0.577 m. The  $D_P$  of the slope is raised step by step with the increase in PGA.

Figures 15 and 16 describe the probability information of  $D_P$  of slope under different  $COV_C$ . The maximum PDF value is 3.2 when the  $COV_C$  is 0.1, and the  $D_P$  is mainly concentrated around 0.2–0.4 m. As the  $COV_C$  improves, the PDF value gradually decreases, the curve gradually shifts to the right, and the  $D_P$  of the slope is more widely distributed. Table 4 shows the information of dynamic reliability of  $D_P$  for the slope when the cumulative slip is 0.05 m, 0.5 m, and 1 m under different  $COV_C$  and PGA values. When the PGA is 0.5 g and the displacement threshold is 1 m, the reliability of the slope subjected to the MAS decreases by 7% with the  $COV_C$  increasing from 0.1 to 0.3. When the  $COV_C$  is 0.3, the dynamic reliability of the slope under the action of the MAS is also reduced by 7% compared with the single mainshock. In addition, with the PGA increasing from 0.4 g to 0.6 g, the reliability of  $D_P$  of the slope produced by the MAS decreased by 8%.



**Figure 14.** Distribution of discrete points of  $D_P$  under different PGA when  $COV_C = 0.3$  (Case 2): (a) PGA = 0.4 g; (b) PGA = 0.6 g.



**Figure 15.** Probability distribution of  $D_P$  with different  $COV_C$  (Case 2): (a) PDF; (b) CDF.

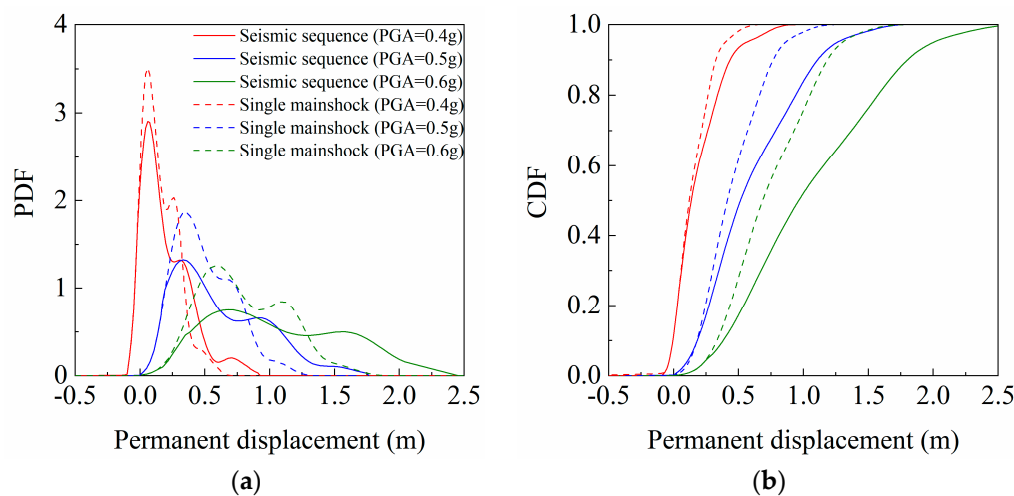
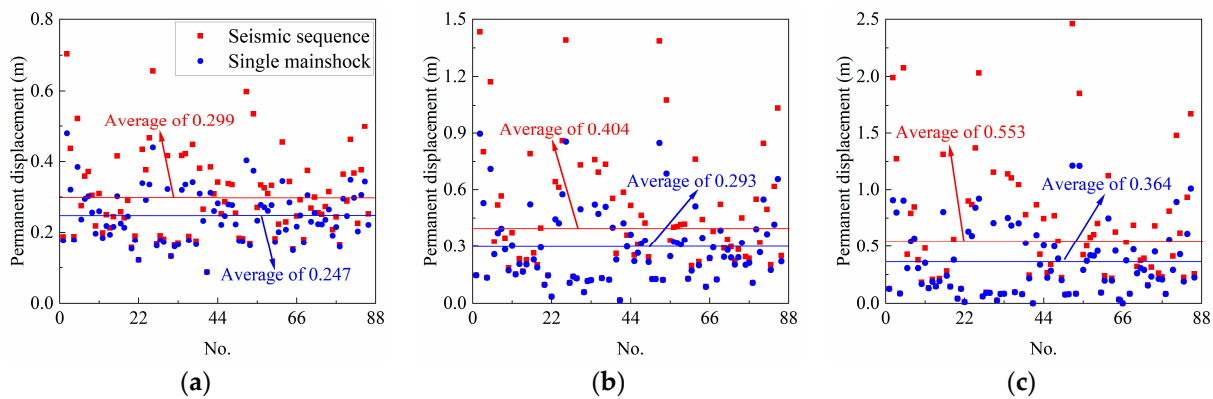


**Figure 16.** Probability distribution of  $D_P$  with different PGA when  $COV_C = 0.3$  (Case 2): (a) horizontal; (b) vertical.

**Table 4.** Dynamic reliability of slope under different  $COV_C$  and PGA (Case 2).

Type of Ground Motion	$D_P$	$COV_C$			PGA		
		0.1	0.2	0.3	0.4 g	0.5 g	0.6 g
Mainshock–aftershock sequence	0.05 m	0	0.02	0.11	0.3	0.11	0.1
	0.5 m	0.97	0.72	0.63	0.94	0.63	0.37
	1 m	1	1	0.93	1	0.93	0.62
Single mainshock	0.05 m	0	0.03	0.11	0.33	0.11	0.1
	0.5 m	1	0.96	0.78	0.98	0.78	0.52
	1 m	1	1	1	1	1	0.92

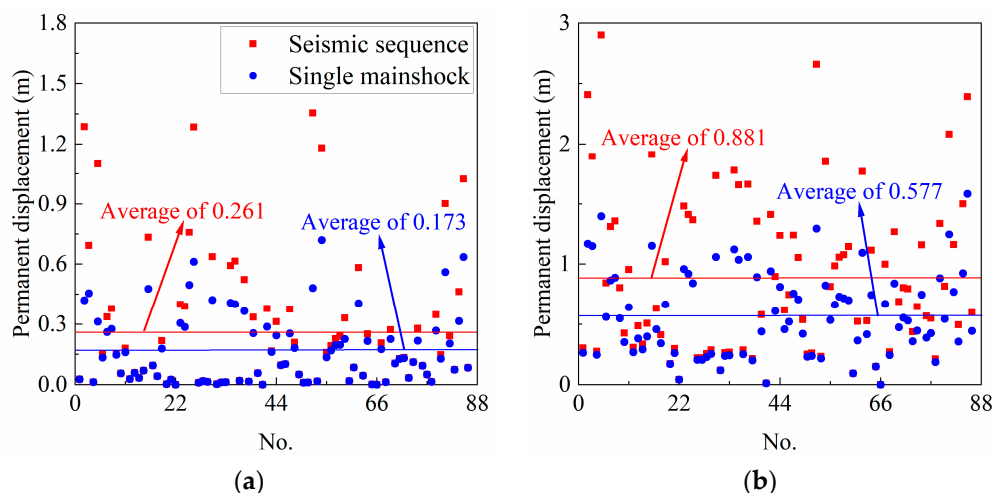
Figure 17 presents the distribution of  $D_P$  discrete points for Case 2 when the  $COV_F$  values are 0.1, 0.2, and 0.3. At a small  $COV_F$  value, the  $D_P$  of the slope is small and concentrated. The variation range of soil increases with the increase in  $COV_F$ , so that the mean of  $D_P$  gradually increases and becomes more discrete. When the  $COV_F$  is 0.1, the mean of  $D_P$  subjected to the MAS is 0.299 m, and the mean of  $D_P$  caused by the single mainshock is 0.247 m. The mean of  $D_P$  under the MAS is larger than that caused by a single mainshock. When the  $COV_F$  values are 0.2 and 0.3, the mean of  $D_P$  produced by MAS is 0.404 m and 0.553 m, respectively. At this time, the mean of  $D_P$  values due to a single mainshock are 0.293 m and 0.364 m. The mean  $D_P$  of the slope keeps increasing with the growth of  $COV_F$ , and the discrepancy of  $D_P$  also displays a gradual increasing tendency.



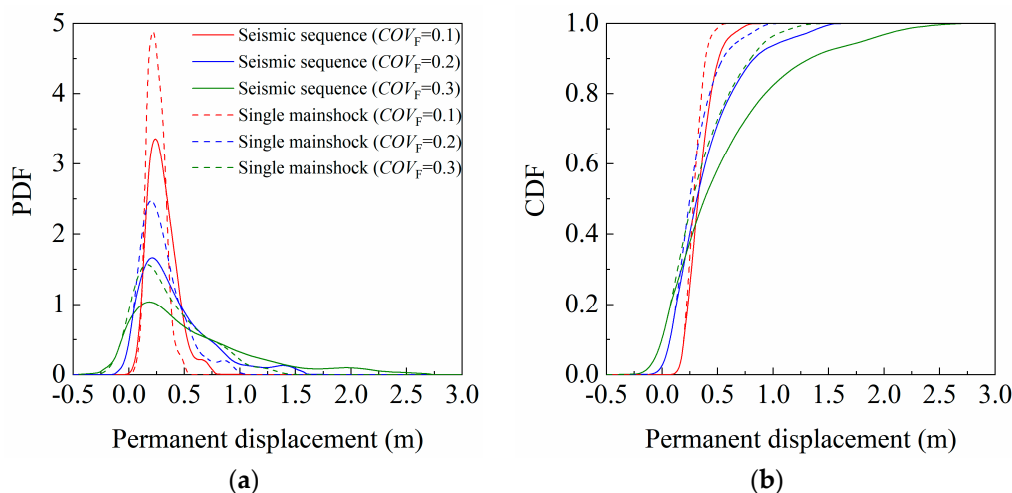
**Figure 17.** Distribution of discrete points of  $D_P$  under different  $COV_F$  (Case 2): (a)  $COV_F = 0.1$ ; (b)  $COV_F = 0.2$ ; (c)  $COV_F = 0.3$ .

Figure 18 shows the distribution of  $D_P$  discrete points of slope under the action of different PGA when the  $COV_F$  is 0.3. When the PGA values are 0.4 g and 0.6 g, the mean of  $D_P$  values of the slope produced by the MAS are 0.261 m and 0.881 m, respectively. However, the mean  $D_P$  values of the slope due to the single mainshock are only 0.173 m and 0.577 m. The  $D_P$  of the slope increases continuously with the increase in PGA.

Figures 19 and 20 show the probability information of  $D_P$  of the slope under different  $COV_F$ . The maximum PDF value is 3.2 when the  $COV_F$  is 0.1, and the  $D_P$  of the slope is mainly focused around 0–0.5 m. The PDF value gradually decreases, the curve gradually shifts to the right with the increase in the  $COV_F$ , and the  $D_P$  of the slope is more widely distributed. Table 5 lists the dynamic reliability of the slope when the cumulative slips are 0.05 m, 0.5 m, and 1 m under  $COV_F$  and PGA. When the PGA is 0.5 g and the threshold is 1 m, the dynamic reliability of the slope induced by the MAS decreases by 17% with the  $COV_F$  increasing from 0.1 to 0.3. When the  $COV_F$  is 0.3, the dynamic reliability of the slope subjected to the MAS is also reduced by 14% compared with the single mainshock. In addition, the dynamic reliability of the slope under the MAS decreased by 14% with the PGA increasing from 0.4 g to 0.6 g.



**Figure 18.** Distribution of discrete points of  $D_P$  under different PGA when  $COV_F = 0.3$  (Case 2): (a) PGA = 0.4 g; (b) PGA = 0.6 g.



**Figure 19.** Probability distribution of  $D_P$  with different  $COV_F$  (Case 2): (a) PDF; (b) CDF.

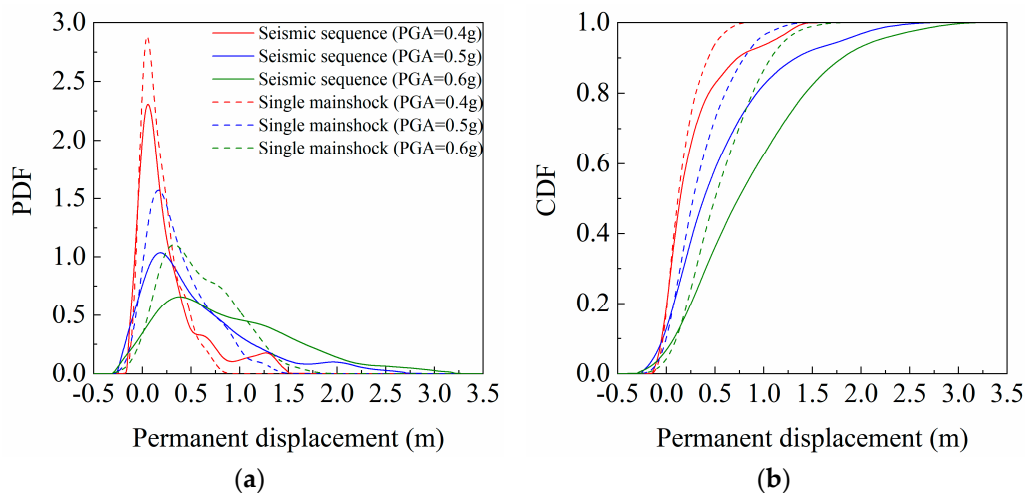


**Figure 20.** Probability distribution of  $D_P$  with different PGA when  $COV_F = 0.3$  (Case 2): (a) PDF; (b) CDF.

**Table 5.** Dynamic reliability of slope under different  $COV_F$  and PGA (Case 2).

Type of Ground Motion	$D_P$	$COV_F$			PGA		
		0.1	0.2	0.3	0.4 g	0.5 g	0.6 g
Mainshock–aftershock sequence	0.05 m	0	0.03	0.18	0.4	0.18	0.05
	0.5 m	0.95	0.74	0.62	0.83	0.62	0.4
	1 m	1	0.94	0.83	0.94	0.83	0.65
Single mainshock	0.05 m	0	0.03	0.19	0.4	0.19	0.06
	0.5 m	1	0.87	0.74	0.95	0.74	0.51
	1 m	1	1	0.97	1	0.97	0.86

On the basis of the above reliability information, it can be seen that the conclusion of Case 1 is comparable to that of Case 2, i.e., the  $COV_F$  has a significantly greater influence on the dynamic reliability of the slope. However, due to the different distribution of soil layers in the layered slopes, the influence of the  $COV$  on the failure probability of a slope is different. Compared with Case 2, the lower layer located on the slope is a sandy soil with poorer properties and its thickness is relatively deep. Therefore, the dynamic reliability of Case 1 is more significantly affected by the  $COV$ . The influence of different soil layers on the dynamic reliability and sliding surface position of slopes has been discussed in our previous research and detailed content can be found in [6].

## 7. Conclusions

A slope reliability analysis method based on GPDEM and the Newmark displacement method is proposed to quantify the impact of spatial variability of soil strength parameters on the dynamic reliability. The MAS and parameter random field are generated by the random simulation method of MAS and spectral representation method. Based on the Newmark method, the  $D_P$  of layered soil slope is calculated by nonintrusive reliability analysis, and the influence of the  $COV_C$  and  $COV_F$  on the dynamic reliability of slope is compared. The conclusions of this study are as follows:

- (1) A reliability analysis method for  $D_P$  of the slope is established based on the GPDEM and Newmark methods. Combined with the noninvasive stochastic analysis method, the failure probability of a slope can be quickly obtained.
- (2) According to the stochastic dynamic calculation results of the layered soil slope,  $COV_C$  and  $COV_F$  have a significant impact on the  $D_P$  of the slope induced by the MAS. The mean of  $D_P$  of the slope also presents a trend of increasing gradually with an increase in the  $COV_C$  and  $COV_F$  values. In contrast, the  $D_P$  of slope is more sensitive to the  $COV_F$ .
- (3) Affected by the randomness and nonlinearity of the materials, the PDF curve has nonuniform single or double peaks. As the  $COV$  increases, the PDF curve becomes lower and wider, and the failure probability of the layered soil slope increases. When the  $D_P$  threshold is 1 m and PGA is 0.5 g, the dynamic reliability of the soil slope is continuously reduced, and the failure probability is even increased by about 20% with the  $COV$  increasing from 0.1 to 0.3.
- (4) The impact of aftershocks on the  $D_P$  of the soil slope cannot be ignored. The mean of  $D_P$  of the slope induced by the MSA is larger than that under a single mainshock. The dynamic reliability of the slope caused by the MAS can even be reduced by 7–30% compared with a single mainshock when the displacement threshold is 1 m and the  $COV_C$  is 0.3. Additionally, the impact of aftershocks on the  $D_P$  of slope increases with an increase in PGA.

**Author Contributions:** Conceptualization, R.P.; Methodology, H.Z.; Software, G.W.; Validation, X.Y.; Writing—original draft, G.W.; Writing—review & editing, R.P.; Supervision, R.P. All authors have read and agreed to the published version of the manuscript.

**Funding:** This work was supported by the National Key Research and Development Program of China (2021YFB2601102), China National Natural Science Foundation (Grant Nos. 52279125, 52279096, and 52009017), and Liaoning Province Science Foundation (2020-BS-06).

**Data Availability Statement:** Not applicable.

**Conflicts of Interest:** The authors declare no conflict of interest.

## References

1. Huang, Y.; Zhao, L.; Li, X. Slope-Dynamic Reliability Analysis Considering Spatial Variability of Soil Parameters. *Int. J. Geomech.* **2020**, *20*, 04020068. [[CrossRef](#)]
2. Huang, J. Chi-Chi earthquake induced landslides in Taiwan. *Earthq. Eng. Eng. Seismol.* **2000**, *2*, 25–33.
3. Xu, C.; Xu, X.; Dai, F. Three (nearly) complete inventories of landslides triggered by the May 12, 2008 Wenchuan Mw 7.9 earthquake of China and their spatial distribution statistical analysis. *Landslides* **2014**, *11*, 441–461. [[CrossRef](#)]
4. Yin, Y.; Zheng, X.; Li, P.; Li, S. Catastrophic landslides associated with the M8.0 Wenchuan earthquake. *Bull. Eng. Geol. Environ.* **2011**, *70*, 35–50. [[CrossRef](#)]
5. Xu, C.; Xu, X. Statistical analysis of landslides caused by the Mw 6.9 Yushu, China, earthquake of April 14, 2010. *Nat. Hazards* **2014**, *72*, 871–893. [[CrossRef](#)]
6. Wang, G.; Pang, R.; Xu, B.; Yu, X. Permanent displacement reliability analysis of soil slopes subjected to mainshock-aftershock sequences. *Comput. Geotech.* **2023**, *153*, 105069. [[CrossRef](#)]
7. Zhang, S.; Wang, G.; Sa, W. Damage evaluation of concrete gravity dams under mainshock-aftershock seismic sequences. *Soil Dyn. Earthq. Eng.* **2013**, *50*, 16–27. [[CrossRef](#)]
8. Liu, J.; Yi, G.; Zhang, Z.; Guan, Z.; Ruan, X.; Long, F.; Du, F. Introduction to the Lushan, Sichuan M7.0 earthquake on 20 April 2013. *Chin. J. Geophys. Chin. Ed.* **2013**, *56*, 1404–1407. [[CrossRef](#)]
9. Kim, B.; Shin, M. A model for estimating horizontal aftershock ground motions for active crustal regions. *Soil Dyn. Earthq. Eng.* **2017**, *92*, 165–175. [[CrossRef](#)]
10. Pang, R.; Xu, B.; Zhou, Y.; Zhang, X.; Wang, X. Fragility analysis of high CFRDs subjected to mainshock-aftershock sequences based on plastic failure. *Eng. Struct.* **2020**, *206*, 110152. [[CrossRef](#)]
11. Zhou, Z.; Yu, X.; Lu, D. Identifying Optimal Intensity Measures for Predicting Damage Potential of Mainshock-Aftershock Sequences. *Appl. Sci.* **2020**, *10*, 6795. [[CrossRef](#)]
12. Shen, J.; Chen, J.; Ding, G. Random field model of sequential ground motions. *Bull. Earthq. Eng.* **2020**, *18*, 5119–5141. [[CrossRef](#)]
13. Jibson, R.W. Methods for assessing the stability of slopes during earthquakes—A retrospective. *Eng. Geol.* **2011**, *122*, 43–50. [[CrossRef](#)]
14. Li, J.; Chen, J. The principle of preservation of probability and the generalized density evolution equation. *Struct. Saf.* **2008**, *30*, 65–77. [[CrossRef](#)]
15. Su, H.; Fu, Z.; Gao, A.; Wen, Z. Numerical simulation of soil levee slope instability using particle-flow code method. *Nat. Hazards Rev.* **2019**, *20*, 04019001. [[CrossRef](#)]
16. Su, H.; Hu, J.; Yang, M.J. Evaluation method for slope stability under multianchor support. *Nat. Hazards Rev.* **2014**, *16*, 04014033. [[CrossRef](#)]
17. Chousianitis, K.; Del Gaudio, V.; Sabatakakis, N.; Kavoura, K.; Drakatos, G.; Bathrellos, G.D.; Skilodimou, H.D. Assessment of earthquake-induced landslide hazard in Greece; from Arias intensity to spatial distribution of slope resistance demand. *Bull. Seismol. Soc. Am.* **2016**, *106*, 174–188. [[CrossRef](#)]
18. Du, W.; Wang, G. A one-step Newmark displacement model for probabilistic seismic slope displacement hazard analysis. *Eng. Geol.* **2016**, *205*, 12–23. [[CrossRef](#)]
19. Wang, M.; Li, D.; Du, W. Probabilistic seismic displacement hazard assessment of earth slopes incorporating spatially random soil parameters. *J. Geotech. Geoenvironmental Eng.* **2021**, *147*, 04021119. [[CrossRef](#)]
20. Li, Y.; Pang, R.; Xu, B.; Wang, X.; Fan, Q.; Jiang, F. GPDEM-based stochastic seismic response analysis of high concrete-faced rockfill dam with spatial variability of rockfill properties based on plastic deformation. *Comput. Geotech.* **2021**, *139*, 104416. [[CrossRef](#)]
21. Pang, R.; Xu, B.; Kong, X.; Zhou, Y.; Zou, D. Seismic performance evaluation of high CFRD slopes subjected to near-fault ground motions based on generalized probability density evolution method. *Eng. Geol.* **2018**, *246*, 391–401. [[CrossRef](#)]
22. Pang, R.; Xu, B.; Zou, D.; Kong, X. Stochastic seismic performance assessment of high CFRDs based on generalized probability density evolution method. *Comput. Geotech.* **2018**, *97*, 233–245. [[CrossRef](#)]
23. Chen, X.; Gao, R.; Gong, W.; Li, Y.; Qiu, J. Random seismic response and dynamic fuzzy reliability analysis of bedding rock slopes based on Pseudoexcitation method. *Int. J. Geomech.* **2018**, *18*, 04017165. [[CrossRef](#)]
24. Liu, L.; Cheng, Y. System reliability analysis of soil slopes using an advanced Kriging metamodel and quasi-Monte Carlo simulation. *Int. J. Geomech.* **2018**, *18*, 06018019. [[CrossRef](#)]
25. Hasofer, A.M.; Lind, N.C. Exact and invariant second-moment code format. *J. Eng. Mech. Div.* **1974**, *100*, 111–121. [[CrossRef](#)]
26. Metropolis, N.; Ulam, S. The monte carlo method. *J. Am. Stat. Assoc.* **1949**, *44*, 335–341. [[CrossRef](#)]
27. Wong, F.S. Slope reliability and response surface method. *J. Geotech. Eng.* **1985**, *111*, 32–53. [[CrossRef](#)]

28. Pasculli, A.; Calista, M.; Sciarra, N. Variability of local stress states resulting from the application of Monte Carlo and finite difference methods to the stability study of a selected slope. *Eng. Geol.* **2018**, *245*, 370–389. [[CrossRef](#)]
29. Li, J.; Chen, J.B. Probability density evolution method for dynamic response analysis of structures with uncertain parameters. *Comput. Mech.* **2004**, *34*, 400–409. [[CrossRef](#)]
30. Li, J.; Chen, J.B. The dimension-reduction strategy via mapping for probability density evolution analysis of nonlinear stochastic systems. *Probabilistic Eng. Mech.* **2006**, *21*, 442–453. [[CrossRef](#)]
31. Huang, Y.; Xiong, M. Dynamic reliability analysis of slopes based on the probability density evolution method. *Soil Dyn. Earthq. Eng.* **2017**, *94*, 1–6. [[CrossRef](#)]
32. Huang, Y.; Hu, H.; Xiong, M. Probability density evolution method for seismic displacement-based assessment of earth retaining structures. *Eng. Geol.* **2018**, *234*, 167–173. [[CrossRef](#)]
33. Pang, R.; Xu, B.; Zhou, Y.; Song, L. Seismic time-history response and system reliability analysis of slopes considering uncertainty of multi-parameters and earthquake excitations. *Comput. Geotech.* **2021**, *136*, 104245. [[CrossRef](#)]
34. Xu, B.; Pang, R.; Zhou, Y. Verification of stochastic seismic analysis method and seismic performance evaluation based on multi-indices for high CFRDs. *Eng. Geol.* **2020**, *264*, 105412. [[CrossRef](#)]
35. Bai, T.; Hu, X.; Gu, F. Practice of searching a noncircular critical slip surface in a slope with soil variability. *Int. J. Geomech.* **2019**, *19*, 04018199. [[CrossRef](#)]
36. Hu, H.; Huang, Y.; Zhao, L. Probabilistic Seismic-Stability Analysis of Slopes Considering the Coupling Effect of Random Ground Motions and Spatially-Variable Soil Properties. *Nat. Hazards Rev.* **2020**, *21*, 04020028. [[CrossRef](#)]
37. Li, D.; Qi, X.; Phoon, K.; Zhang, L.; Zhou, C. Effect of spatially variable shear strength parameters with linearly increasing mean trend on reliability of infinite slopes. *Struct. Saf.* **2014**, *49*, 45–55. [[CrossRef](#)]
38. Hariri-Ardebili, M.A.; Seyed-Kolbadi, S.M.; Saouma, V.E.; Salamon, J.; Rajagopalan, B. Random finite element method for the seismic analysis of gravity dams. *Eng. Struct.* **2018**, *171*, 405–420. [[CrossRef](#)]
39. Zhang, J.; Zhang, M.; Tang, W. New methods for system reliability analysis of soil slopes. *Can. Geotech. J.* **2011**, *48*, 1138–1148. [[CrossRef](#)]
40. Cornell, A. *First-Order Uncertainty Analysis of Soil Deformation and Stability*; Publication of University of Hong Kong: Hong Kong, China, 1972.
41. Vanmarcke, E. Reliability of earth slopes. *J. Geotechnical Eng.* **1977**, *103*, 1247–1265. [[CrossRef](#)]
42. Der Kiureghian, A.; Ke, J. The stochastic finite element method in structural reliability. *Probabilistic Eng. Mech.* **1988**, *3*, 83–91. [[CrossRef](#)]
43. Shinozuka, M.; Deodatis, G. Simulation of multi-dimensional Gaussian stochastic fields by spectral representation. *Appl. Mech. Rev.* **1996**, *49*, 29–53. [[CrossRef](#)]
44. Matthies, H.G.; Brenner, C.E.; Bucher, C.G.; Guedes Soares, C. Uncertainties in probabilistic numerical analysis of structures and solids-Stochastic finite elements. *Struct. Saf.* **1997**, *19*, 283–336. [[CrossRef](#)]
45. Ghiocel, D.; Ghanem, R. Stochastic finite-element analysis of seismic soil-structure interaction. *J. Eng. Mech.* **2002**, *128*, 66–77. [[CrossRef](#)]
46. Pang, R.; Zhou, Y.; Chen, G.; Jing, M. Stochastic mainshock-aftershock simulation and its applications in dynamic reliability of structural systems via DPIM. *J. Eng. Mech.* **2023**, *149*, 04022096. [[CrossRef](#)]
47. Huang, L. *Dynamic Stability Analysis of Layered Soil Slope under Earthquake*; Southwest Jiaotong University: Chengdu, China, 2017. (In Chinese)
48. Ching, J.; Phoon, K. Effect of element sizes in random field finite element simulations of soil shear strength. *Comput. Struct.* **2013**, *126*, 120–134. [[CrossRef](#)]

**Disclaimer/Publisher’s Note:** The statements, opinions and data contained in all publications are solely those of the individual author(s) and contributor(s) and not of MDPI and/or the editor(s). MDPI and/or the editor(s) disclaim responsibility for any injury to people or property resulting from any ideas, methods, instructions or products referred to in the content.